PNAS RESEARCH ARTICLE | NEUROSCIENCE OPEN ACCESS

Synaptotagmin-1 is a bidirectional Ca^{2+} sensor for neuronal endocytosis

Yang Chen[a,b,1], Shaoqin Hu[a,1], Xuanang Wu[a,1], Zhenli Xie[a,c,d,e,1], Yuan Wang[d,e], Bianbian Wang[a,f], Xiaopeng Li[a,f], Yingmei Pei[a], Yuhao Gu[a], Kai Huang[a,g], Jingxiao Huo[a], Anqi Wei[a], Cheng Bi[a], Zhe Lu[a], Qian Song[a], Huadong Xu[h], Xinjiang Kang[f,h], Shuli Shao[i], Jiangang Long[a], Jiankang Liu[a], Zhuan Zhou[d,e], Rong Huang[d,e,2], Zuying Chai[d,e,2], and Changhe Wang[a,b,c,h,2]

Edited by Won Do Heo, Korea Advanced Institute of Science and Technology, Daejeon, South Korea; received June 15, 2021; accepted April 6, 2022 by Editorial Board Member Hee-Sup Shin

Exocytosis and endocytosis are tightly coupled. In addition to initiating exocytosis, Ca^{2+} plays critical roles in exocytosis–endocytosis coupling in neurons and nonneuronal cells. Both positive and negative roles of Ca^{2+} in endocytosis have been reported; however, Ca^{2+} inhibition in endocytosis remains debatable with unknown mechanisms. Here, we show that synaptotagmin-1 (Syt1), the primary Ca^{2+} sensor initiating exocytosis, plays bidirectional and opposite roles in exocytosis–endocytosis coupling by promoting slow, small-sized clathrin-mediated endocytosis but inhibiting fast, large-sized bulk endocytosis. Ca^{2+}-binding ability is required for Syt1 to regulate both types of endocytic pathways, the disruption of which leads to inefficient vesicle recycling under mild stimulation and excessive membrane retrieval following intense stimulation. Ca^{2+}-dependent membrane tubulation may explain the opposite endocytic roles of Syt1 and provides a general membrane-remodeling working model for endocytosis determination. Thus, Syt1 is a primary bidirectional Ca^{2+} sensor facilitating clathrin-mediated endocytosis but clamping bulk endocytosis, probably by manipulating membrane curvature to ensure both efficient and precise coupling of endocytosis to exocytosis.

synaptotagmin | clathrin-mediated endocytosis | bulk endocytosis | Ca^{2+} | membrane tubulation

Endocytosis and subsequent vesicle recycling are spatiotemporally coupled to exocytosis, which is critical for neurons and endocrinal cells to maintain the integrity of plasma membrane architecture, intracellular homeostasis, and sustained neurotransmission (1–3). In addition to triggering vesicular exocytosis, neural activity/Ca^{2+} also play an executive role in the coupling of endocytosis to exocytosis (1, 2, 4–6). Following a pioneering study 40 y ago (7), extensive studies have been conducted and showed that Ca^{2+} triggers and facilitates vesicle endocytosis in neurons and nonneuronal secretory cells (1, 8–11). Accumulating evidence also shows that intracellular Ca^{2+} may inhibit endocytosis (12–15), which has been challenged greatly due to the apparently lower occurrences in few preparations and the missing underlining mechanisms, making the endocytic role of Ca^{2+} a four-decades–long dispute (1, 2, 4, 6).

Machineries and regulators involved in exocytosis–endocytosis coupling have been extensively studied for over 30 y. The soluble *N*-ethylmaleimide–sensitive factor attachment protein receptors (SNAREs) and synaptophysin play critical dual roles in exocytosis and endocytosis during neurotransmission (2, 3, 16, 17). Calmodulin and synaptotagmin-1 (Syt1) are currently known primary Ca^{2+} sensors facilitating endocytosis (1, 9, 16, 18, 19). Ca^{2+}/calmodulin activate calcineurin, which dephosphorylates endocytic proteins (e.g., dynamin, synaptojanin, and amphiphysin) to facilitate clathrin-mediated endocytosis (CME) and clathrin-independent fast endocytosis (1, 2). Syt1 is a dual Ca^{2+} sensor for both exocytosis and endocytosis (5, 16, 18–20). It promotes CME through binding with the endocytic adaptors adaptor protein-2 (AP-2) and stonin-2 (21–24). In contrast to the well-established Ca^{2+} sensors that promote endocytosis, the mechanism of Ca^{2+}-dependent inhibition in endocytosis remains unknown.

CME is the classical but slow endocytosis pathway for vesicle retrieval under resting conditions or in response to mild stimulation, while the accumulated Ca^{2+} also triggers calmodulin/calcineurin-dependent bulk endocytosis, which takes up a large area of plasma membrane to fulfill the urgent requirement for high-speed vesicle exocytosis (1–3). They cooperate with kiss-and-run and ultrafast endocytosis to ensure both sufficient and precise membrane retrieval following exocytosis (3, 25–27). These endocytic pathways are all initiated from membrane invagination and are critically controlled by neural activity. However, how the switch between different endocytic modes is precisely determined remains largely unknown.

Significance

Precise and efficient coupling of endocytosis to exocytosis is critical for neurotransmission. The activity-dependent facilitation of endocytosis has been well established for efficient membrane retrieval; however, whether neural activity clamps endocytosis to avoid excessive membrane retrieval remains debatable with the mechanisms largely unknown. The present work provides compelling evidence that synaptotagmin-1 (Syt1) functions as a primary bidirectional Ca^{2+} sensor to promote slow, small-sized clathrin-mediated endocytosis but inhibit the fast, large-sized bulk endocytosis during elevated neural activity, the disruption of which leads to inefficient vesicle recycling under mild stimulation but excessive membrane retrieval following sustained neurotransmission. Thus, Syt1 serves as a fine-tuning Ca^{2+} sensor to ensure both efficient and precise coupling of endocytosis to exocytosis in response to different neural activities.

The authors declare no competing interest.

This article is a PNAS Direct Submission. W.D.H. is a guest editor invited by the Editorial Board.

[1]Y.C., S.H., X.W., and Z.X. contributed equally to this work.

[2]To whom correspondence may be addressed. Email: changhewang@xjtu.edu.cn, 748548830@qq.com, or strive0920@163.com.

This article contains supporting information online at http://www.pnas.org/lookup/suppl/doi:10.1073/pnas.2111051119/-/DCSupplemental.

Published May 10, 2022.

Here, by combining electrophysiological recordings, confocal live imaging, superresolution stimulated emission depletion (STED) imaging, in vitro liposome manipulation, and electron microscope imaging of individual endocytic vesicles, we define Syt1 as a primary and bidirectional Ca^{2+} sensor for endocytosis, which promotes CME but inhibits bulk endocytosis, probably by mediating membrane remodeling. The balance between the facilitatory and inhibitory effects of Syt1 on endocytosis offers a fine-tuning mechanism to ensure both efficient and precise coupling of endocytosis to exocytosis. By including a non-Ca^{2+}–binding Syt as the constitutive brake, this work also explains the four-decades–long puzzle about the positive and negative Ca^{2+} effects on endocytosis.

Results

Syt1 Bidirectionally Regulates Endocytosis during Synaptic Transmission. Syt1 is a well-established primary Ca^{2+} sensor that triggers vesicular exocytosis by forming the fusion machinery with the SNARE complex and plasma membrane (5). To determine whether Syt1 is also involved in exocytosis–endocytosis coupling during neurotransmission, we performed live imaging of synaptophysin–pHluorin (Syp–pH) (3, 28) in hippocampal nerve terminals with or without Syt1 knockdown (KD) (Fig. 1 A and B). Due to lower transfection efficiency in neurons, the KD efficiency and rescue effects were confirmed by Western blot in HEK cells and immunofluorescence in dorsal root ganglion (DRG) and hippocampal neurons (*SI Appendix*, Fig. S1). Consistent with previous reports (21, 22), Syt1-KD neurons showed a decreased endocytic rate with a longer time constant following weak depolarization with 45 mM KCl stimulation (10 s; *SI Appendix*, Figs. S2 and S3), confirming the facilitatory role of Syt1 in synaptic endocytosis. In contrast, the endocytic fluorescence decay was greatly accelerated in Syt1-KD neurons during prolonged and elevated neuronal activity (30 s of 70 mM KCl; Fig. 1 A–E and *SI Appendix*, Fig. S2), which was shown to trigger bulk endocytosis (26, 29). The fluorescence decay fitted well to a double-exponential function, and the initial fast phase was greatly accelerated by Syt1 KD while the subsequent slow phase decreased significantly (Fig. 1 F–H), suggesting that Syt1 inhibits the fast component but promotes the slow phase of endocytosis during sustained neuronal activity. In addition, Syt1 KD also induced the reduction of fluorescence increase (*SI Appendix*, Fig. S4) and greatly increased the probability of fluorescence overshoot following endocytosis (Fig. 1 I and J), representing the disturbance of exocytosis–endocytosis coupling and excessive membrane retrieval after exocytosis. Importantly, the KD effect was fully rescued by overexpressing a short hairpin RNA (shRNA)–resistant form of Syt1 (Fig. 1 and *SI Appendix*, Figs. S1, S3, and S4), demonstrating the bidirectional role of Syt1 in synaptic endocytosis.

Consistently, patch clamp membrane capacitance (C_m) recordings showed a similar endocytic role of Syt1 following the somatic secretion of the primary sensory DRG neurons. The endocytic rate of Syt1-KD neurons was much slower under mild stimulation (single-pulse depolarization) but faster under intense (2-Hz train) stimulation than in control neurons (*SI Appendix*, Fig. S5 *A–D*). Similarly, following sustained stimulation, the fast phase of C_m decay was greatly accelerated by Syt1 KD, while the subsequent slow phase decreased significantly (*SI Appendix*, Fig. S5 *E–G*), confirming that Syt1 inhibits the fast component but promotes the slow phase of endocytosis during elevated neuronal activity. Consistent with Syp–pH imaging in synaptic boutons, Syt1 KD substantially increased the probability of C_m overshoot (*SI Appendix*, Fig. S5 *C*), suggesting the requirement of Syt1 in maintaining the balance of exocytosis–endocytosis, especially during sustained neuronal activity. As expected, the endocytic defects in KD neurons were fully rescued by full-length Syt1 (*SI Appendix*, Fig. S5). Thus, Syt1 bidirectionally regulates endocytosis during neurotransmission.

Syt1 Differentially Regulates Endocytosis of Small-Sized and Large-Sized Vesicles. To further characterize the role of Syt1 in exocytosis–endocytosis coupling, we imaged fixed hippocampal neurons after performing dextran (10 kDa) uptake and compared the sizes of individual endocytic vesicles in KD and control synaptic boutons with STED superresolution (~40-nm) microscopy (30, 31). Syp–pH was expressed to indicate vesicular organelles, and the fluorescent dextran spots surrounded by Syp–pH rings were identified as endocytic vesicles (Fig. 2 A and B). In control and rescue boutons, we observed a single population of small endocytic vesicles with a diameter of ~50 nm (Fig. 2 C–F), which remained intact in Syt1-KD boutons under resting conditions (*SI Appendix*, Fig. S6 *A–C*). In contrast, an additional group of large-sized endocytic vesicles (~110 nm) were observed in KD boutons in response to 70 mM KCl stimulation (Fig. 2 C–F), suggesting the increased occurrence of activity-dependent bulk endocytosis in the absence of Syt1. Consistently, both the density and proportion of endocytic small vesicles ($\Phi \leq 65$ nm) decreased, while that of large endocytic vesicles ($\Phi > 65$ nm) increased greatly in KD boutons under elevated neuronal activity (Fig. 2 G and H and *SI Appendix*, Fig. S6 *D* and *E*), suggesting critical roles of Syt1 in facilitating small-sized, but clamping large-sized, vesicular endocytosis.

To further confirm the bidirectional roles of Syt1 in exocytosis–endocytosis, we performed the conditional knockout (cKO) of Syt1 by infecting hippocampal neurons from homozygous floxed Syt1-null mice with Cre recombinase–carrying AAV2/9 virus (Fig. 3A). The $FLEx^{loxP}$-based Syp–pH-overexpressing virus was codelivered with Cre virus for the real-time visualization of synaptic exocytosis–endocytosis (Fig. 3A). Consistently, Syt1-cKO boutons showed a decreased endocytic rate following depolarization with 45 mM KCl (Fig. 3 B–D), while fluorescence decay was greatly accelerated following 70 mM KCl stimulation (Fig. 3 E and F). Similarly, the fluorescence decay in Syt1-cKO boutons also fitted well to a double-exponential function (Fig. 3 E and F), where the initial fast phase greatly accelerated and the subsequent slow phase decreased (Fig. 3 E–H). The phenomenon was further confirmed in Syt1-cKO hippocampal neurons elicited with electrical stimuli (mimicking action potentials) at physiological temperature (*SI Appendix*, Fig. S7), confirming the bidirectional roles of Syt1 in fast versus slow endocytosis during synaptic transmission. Upon STED imaging of synaptic boutons following stimulus-coupled dextran (10-kDa) uptake, we confirmed the single population of small endocytic vesicles in controls (Fig. 3 I and J), while an additional group of large-sized vesicles was observed in Syt1-cKO boutons (Fig. 3 I and K). Furthermore, the number and proportion of small endocytic vesicles decreased greatly while that of large endocytic vesicles increased in Syt1-cKO boutons (Fig. 3 L and M). Importantly, horseradish peroxide (HRP) uptake and transmission electron microscopy imaging showed decreased HRP-labeled small vesicles and the appearance of bulk-like large endosome structures in Syt1-cKO hippocampal synapses (Fig. 3 N–P). Collectively, these results demonstrate that Syt1 promotes small-sized

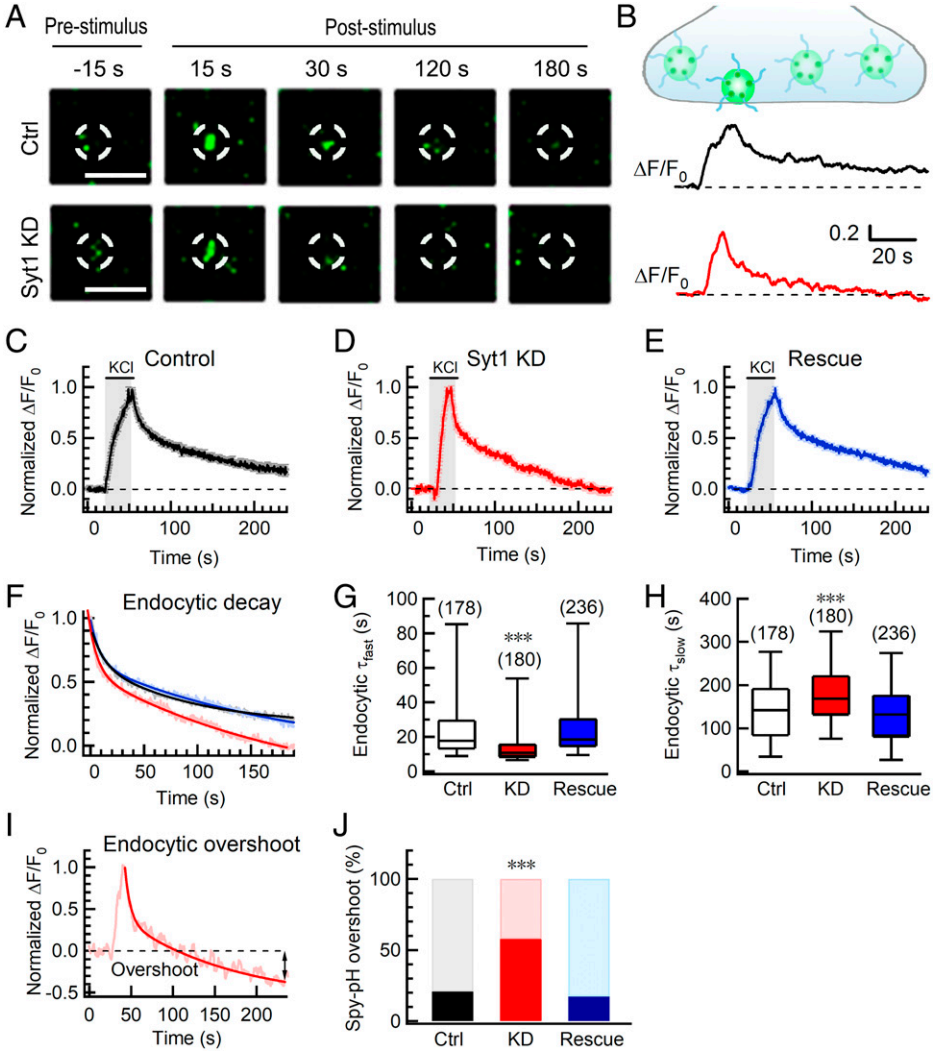

Fig. 1. Syt1 bidirectionally regulates the fast and slow phases of endocytosis in synaptic boutons. (*A*) Sample images showing Syp–pH fluorescence in presynaptic boutons of scrambled shRNA control (Ctrl) or Syt1-KD hippocampal neurons 15 s before, 15 s, 30 s, 120 s, and 180 s after KCl stimulation. (Scale bars, 5 μm.) (*B*) Cartoon illustration and fluorescence changes ($\Delta F/F_0$) showing the real-time imaging of Syp–pH during exocytosis and endocytosis as in *A*. (*C–E*) Normalized fluorescence changes (mean ± SEM) of Syp–pH in control (*C*; $n = 178$), Syt1-KD (*D*; $n = 180$), and rescue (*E*; $n = 236$) hippocampal synapses in response to 70 mM KCl stimulation (30 s). (*F*) The overlaid fluorescence endocytic decay as in *C–E*. The traces were fitted to a double-exponential function (solid traces). (*G* and *H*) Fast (*G*) and slow (*H*) time constants of endocytosis recorded as in *C–E*. (*I* and *J*) Representative fluorescence trace (*I*) and statistics (*J*) of endocytic overshoot in hippocampal neurons. Error bars indicate SEM. In the box plots, the central line of each box represents the median, the edges of the box represent the 25th and 75th percentiles, and the whiskers extend to the 5th and 95th data points. Data were collected from six independent experiments. A one-way ANOVA (*G* and *H*) or Fisher's exact test (*J*) was performed; ***$P < 0.001$.

(slow phase), but inhibits large-sized (fast phase), vesicular endocytosis during neurotransmission.

Syt1 Is a Ca^{2+} Sensor Facilitating CME but Inhibiting Bulk Endocytosis. CME is a classical but slow endocytosis pathway with small-sized (~50-nm) endocytic vesicles (32), while accumulated Ca^{2+} also triggers calmodulin-dependent bulk endocytosis (*SI Appendix*, Fig. S8 and refs. 26 and 33), which forms large intracellular endosomes with diameters of over 100 nm. Syt1 is known to promote CME via binding to AP-2 and stonin-2 (3, 5, 16, 18, 24, 34); however, whether and how Syt1 is involved in bulk endocytosis regulation remains unknown. Nonetheless, the increased vesicle size at rest and abundant large endosome structures following stimulation in Syt1-KO synapses imply a possible inhibitory role of Syt1 in bulk endocytosis (21, 35). Thus, we hypothesized that Syt1 functions as a bidirectional Ca^{2+} sensor to promote CME but inhibit bulk endocytosis during neurotransmission.

To test this hypothesis, we used transferrin (Tf) uptake (Fig. 4A) to assess CME and large dextran (40-kDa) uptake (Fig. 4G) to quantify bulk endocytosis in the somata of DRG neurons (25, 26). We found that Tf uptake was greatly accelerated by increasing the $[Ca^{2+}]_o$ (extracellular Ca^{2+} concentration) from 2.5 to 10 mM (Fig. 4B and *SI Appendix*, Fig. S9*A*) but diminished by the preloading of a membrane-permeable potent Ca^{2+} chelator 1,2-Bis (2-aminophenoxy) ethane-N,N,N′,N′-tetraacetic acid tetrakis, acetoxymethyl ester (BAPTA-AM) (Fig. 4C and *SI Appendix*, Fig. S9*B*). Electron microscopy experiments showed the Ca^{2+}-dependent increase of clathrin-coated pits and bulk-like structures along the plasma membrane (*SI Appendix*, Figs. S9 and S10*A*). Similarly, the internalized puncta of 40-kDa dextran increased greatly following elevated $[Ca^{2+}]_i$ (intracellular Ca^{2+} concentration) upon KCl stimulation (Fig. 4H). Furthermore, under 2-Hz train stimulation, transient application of 10 mM $[Ca^{2+}]_o$ increased the frequency of bulk endocytic events and sped up the fission rate of single bulk events, leaving exocytosis mainly unchanged (*SI*

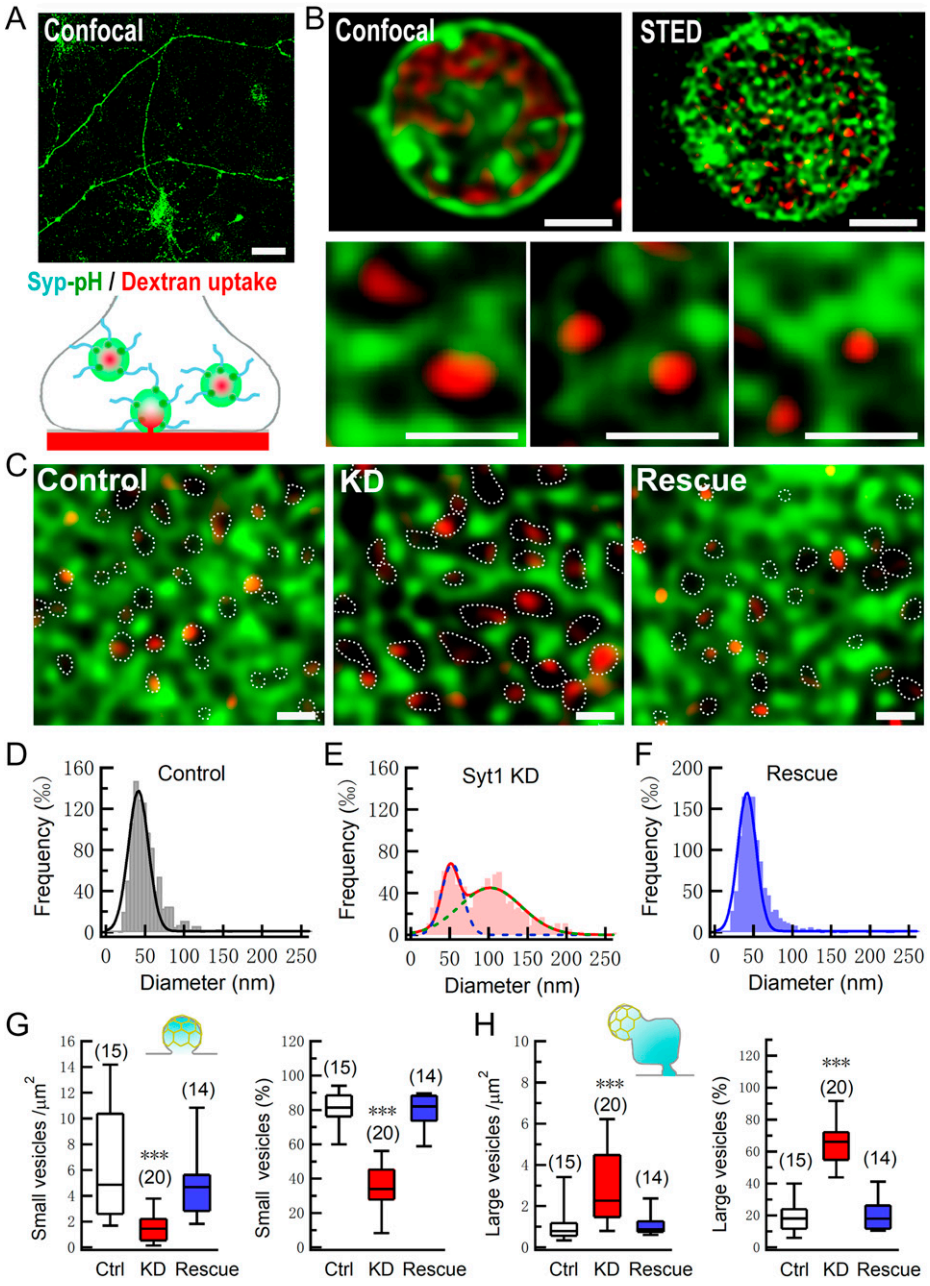

Fig. 2. Syt1 bidirectionally regulates small- and large-sized endocytosis in synaptic boutons. (*A* and *B*) Cartoon illustration and sample images showing the confocal and STED imaging of Syp–pH and endocytosed dextran (10 kDa) in hippocampal synaptic boutons following KCl stimulation. Endocytic vesicles were identified as dextran-positive (red) Syp–pH rings (green) as indicated in *B* (*Bottom*). (Scale bars, 20 μm [*A*], 1 μm [*B*, *Top*], and 200 nm [*B*, *Bottom*]). (*C–F*) Representative micrographs and histogram showing the size of endocytic vesicles (dextran-positive) in scrambled control, Syt1-KD, and rescue boutons following 70 mM KCl stimulation (2 min). (Scale bar, 100 nm.) The dashed and solid traces in *D–F* are the individual and overall fits to single or multiple (KD with KCl stimulation) Gaussian functions. A single peak at ~50 nm in *D* and *F* and multiple peaks at ~50 and ~105 nm in *E* are shown. (*G* and *H*) Statistics of small (*G*; $\Phi \leq 65$ nm) and large (*H*; $\Phi > 65$ nm) endocytic vesicles in scrambled control, Syt1-KD, and rescue boutons following 70 mM KCl stimulation as in *C–F*. Data were collected from four independent experiments and were analyzed by one-way ANOVA; ***$P < 0.001$.

Appendix, Fig. S10 *B–E*). These data validate that CME and bulk endocytosis in peripheral neurons are Ca^{2+} dependent.

Next, we determined whether Syt1 functions as a Ca^{2+} sensor to regulate CME and bulk endocytosis (25, 26). As expected, Syt1 KD significantly reduced Tf uptake (Fig. 4 E and F) but increased large dextran uptake (Fig. 4 I and J), which were completely rescued by full-length Syt1. Consistently, Syt1-cKO DRG neurons also showed decreased Tf uptake and increased large dextran uptake (*SI Appendix*, Fig. S11), confirming our hypothesis that Syt1 facilitates CME but inhibits bulk endocytosis in neurons.

To determine whether Ca^{2+}-binding activity is critical for Syt1 to regulate exocytosis–endocytosis, two Ca^{2+} ligands in the C2A and/or C2B domain of Syt1 were neutralized by substituting the native aspartic acid (Asp) residues with asparagines (Asn) to attenuate Ca^{2+}-binding ability (Fig. 4D) (16). All mutants showed similar expression levels with that of wild-type Syt1 (*SI Appendix*, Fig. S1). As expected, complete abolishment of Ca^{2+}-binding ability (C2A*–C2B*) prevented Syt1 from rescuing both Tf and dextran uptake in KD neurons (Fig. 4 F and J), demonstrating that Syt1 functions as a Ca^{2+} sensor to promote CME but inhibit bulk endocytosis. Either the

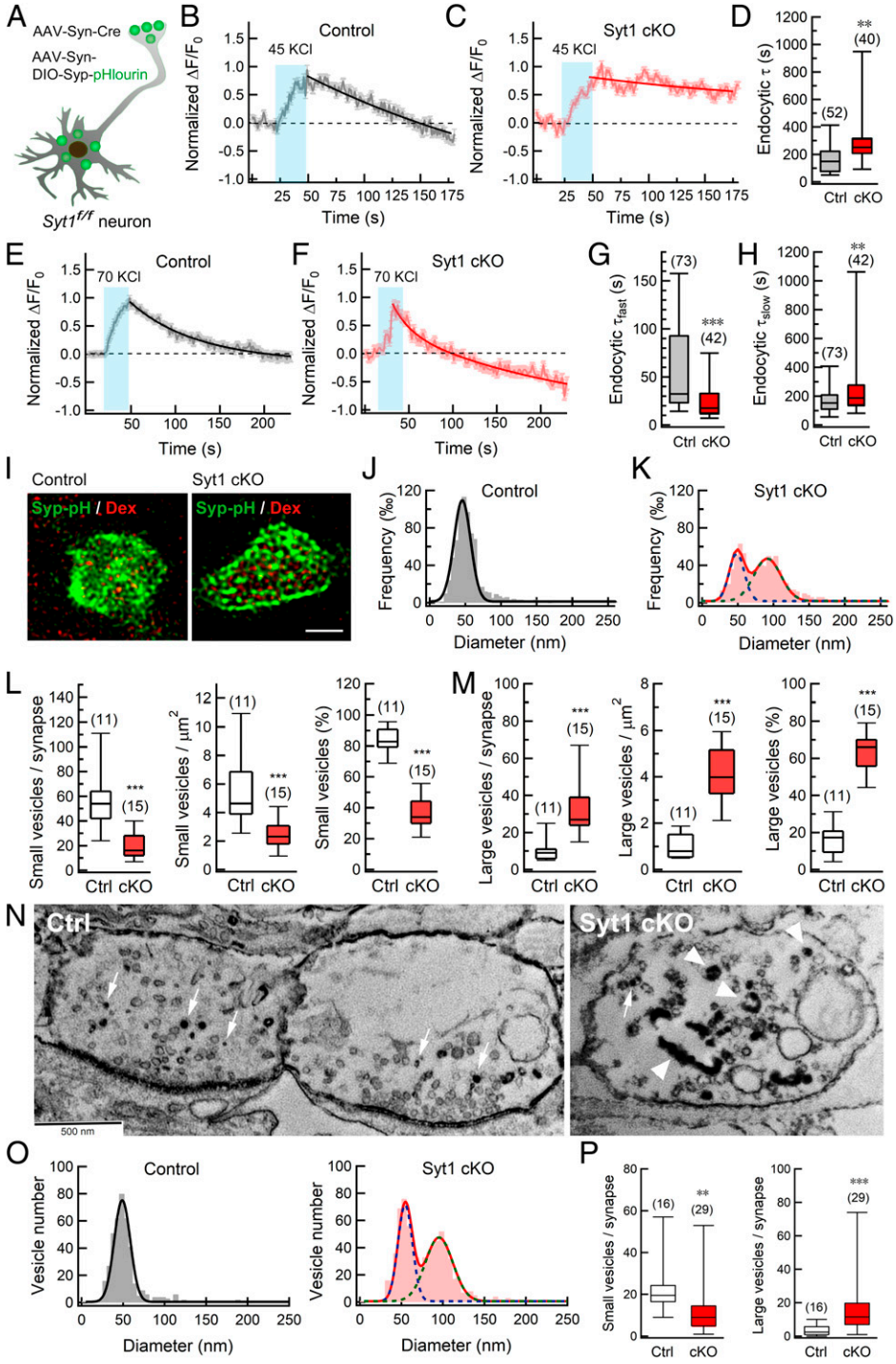

Fig. 3. Syt1 promotes slow-phase small-sized endocytosis but inhibits fast-phase large-sized endocytosis in synaptic boutons. (*A*) Cartoon illustration of viral infection for the Cre-dependent knockout of Syt1 and specific expression of Syp–pH in *Syt1*$^{f/f}$ hippocampal neurons. (*B* and *C*) Normalized fluorescence changes (mean ± SEM) of Syp–pH in control (*B*) and Syt1-cKO (*C*) synapses in response to 45 mM KCl stimulation. The traces were fitted to an exponential function (solid traces). (*D*) The time constant of endocytosis recorded as in *B* and *C*. (*E* and *F*) Normalized fluorescence changes (mean ± SEM) of Syp–pH in control (*E*) and Syt1-cKO (*F*) synapses in response to 70 mM KCl stimulation. The traces were fitted to a double-exponential function (solid traces). (*G* and *H*) Fast (*G*) and slow (*H*) time constants of endocytosis recorded as in *E* and *F*. (*I*) Representative micrographs showing the STED imaging of Syp–pH and endocytosed dextran (10 kDa) in Syt1-cKO hippocampal synaptic boutons following 70 mM KCl stimulation (2 min). (Scale bar, 1 μm.) (*J* and *K*) Histograms showing the diameter distribution of endocytic vesicles (dextran-positive) in control (*J*) and Syt1-cKO (*K*) boutons as in *I*. The dashed and solid traces are the individual and overall fits to single (control) or multiple (cKO) Gaussian functions. (*L* and *M*) Statistics of small (*L*; $\Phi \leq 65$ nm) and large (*M*; $\Phi > 65$ nm) endocytic vesicles in control and Syt1-cKO boutons following 70 mM KCl stimulation as in *I*–*K*. (*N*) Representative electron micrographs of HRP uptake following 2-min 100 mM K^+ stimulation. (Scale bar, 500 nm.) (*O* and *P*) Statistics of small endocytic vesicles ($\Phi \leq 65$ nm, arrows) and large endosomes ($\Phi > 65$ nm, arrowheads) in control and Syt1-cKO boutons as in *N*. In the box plots, the central line of each box represents the median, the edges of the box represent the 25th and 75th percentiles, and the whiskers extend to the most extreme data points. Data were collected from four to five independent experiments and were analyzed by Mann–Whitney *U* test; $^{**}P < 0.01$, $^{***}P < 0.001$.

C2A-only (C2A*–C2B) or the C2B-only (C2A–C2B*) mutation restored the KD-decreased Tf uptake (Fig. 4F), indicating that the Ca^{2+}-binding sites of the C2A and C2B domains are redundant for CME, consistent with previous studies (16). In contrast, large dextran uptake was critically dependent on the Ca^{2+}-binding site of the C2B domain only but not the C2A

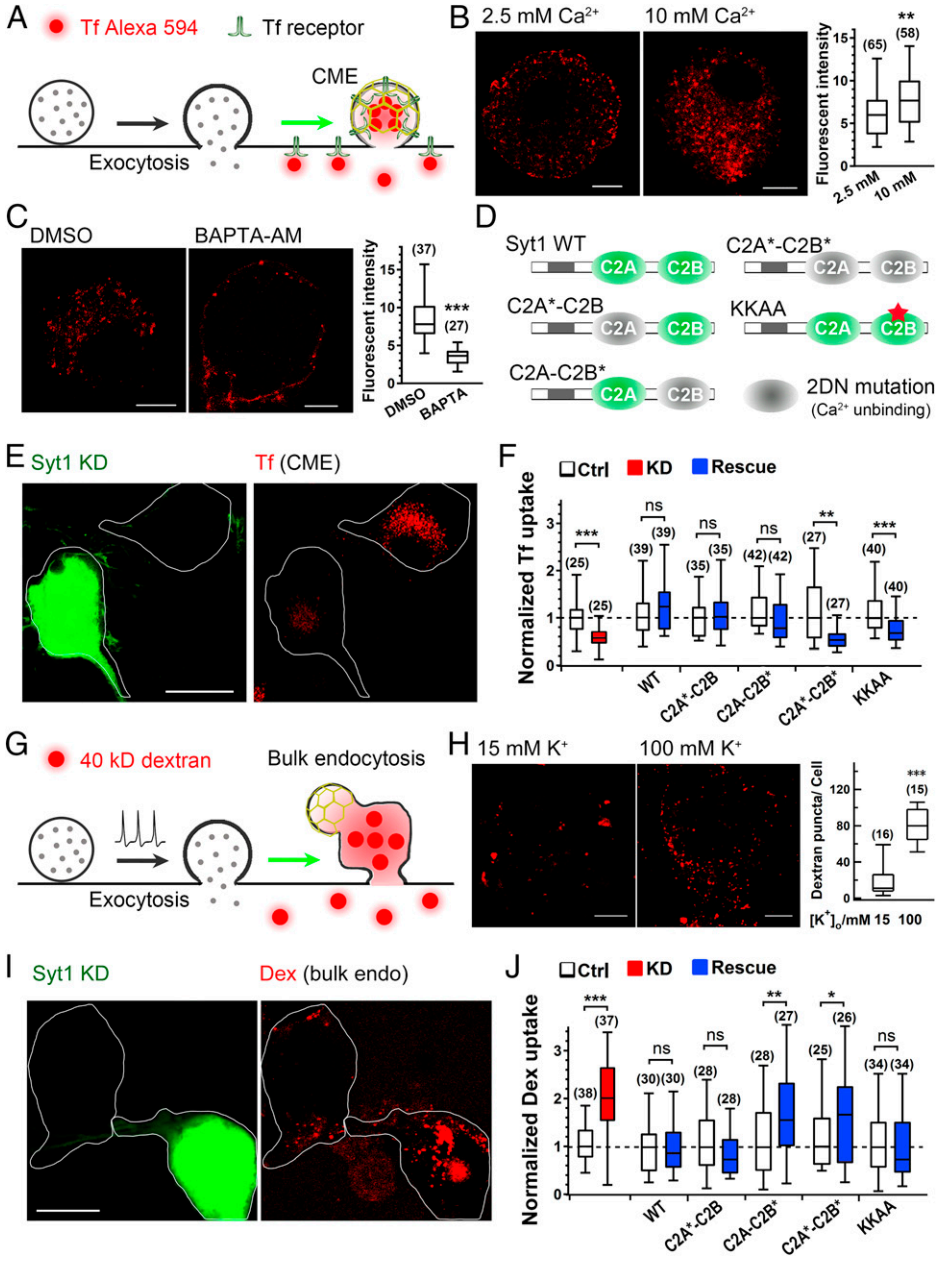

Fig. 4. Syt1 is a Ca^{2+} sensor facilitating CME but inhibiting bulk endocytosis in neuronal somata. (*A*) Cartoon illustration of Tf uptake through CME. (*B*) Tf uptake in DRG neurons in 2.5 or 10 mM $[Ca^{2+}]_o$. *Right*, quantification of Tf fluorescence density. (*C*) As in *B*, but with 0.1% dimethyl sulfoxide (DMSO; control) or BAPTA-AM (with DMSO) in the 2.5 mM Ca^{2+} solution. (*D*) Diagram of the mutant forms of Syt1 used for rescue experiments (wild-type, 2DN [*] mutants in C2A and/or C2B, or KKAA mutant). (*E* and *F*) Representative images (*E*) and quantification (*F*) of Tf uptake in control and Syt1-KD DRG neurons with or without rescue by the indicated forms of Syt1. (*G*) Cartoon illustration of large dextran (40 kDa) uptake through bulk endocytosis. (*H*) Representative *z*-projected fluorescence images (*Left*) showing 40-kDa dextran uptake in DRG neurons stimulated with 15 or 100 mM K^+. Quantification is shown on the *Right*. (*I* and *J*) Representative *z*-projected fluorescence images (*I*) and statistics (*J*) of large dextran (Dex) uptake by control and Syt1-KD DRG neurons with or without rescue by the indicated forms of Syt1. (Scale bars, 5 μm [*B* and *C*], 10 μm [*H*], and 20 μm [*E* and *I*]). In the box plots, the central line of each box represents the median, the edges of the box represent the 25th and 75th percentiles, and the whiskers extend to the most extreme data points. Data were collected from three to five independent experiments and were analyzed by Mann–Whitney *U* test; $*P < 0.05$, $**P < 0.01$, $***P < 0.001$; ns, not significant.

domain (Fig. 4J). The conserved poly-lysine region of the C2B domain, which has been shown to affect CME by binding to AP-2 and stonin-2 (16, 24), was essential for Tf uptake but not dextran uptake (KKAA mutant; Fig. 4 D, F, and J). These findings demonstrate the critical roles of Syt1 as a primary Ca^{2+} sensor to promote CME and inhibit bulk endocytosis during somatic secretion.

To further confirm the function of Syt1 in synaptic endocytosis, we performed similar rescue experiments on Syt1-KD hippocampal nerve terminals (Fig. 5A), which was shown to have reduced small-sized vesicles but increased large-sized vesicles (Fig. 2). Similarly, either the C2A*–C2B or the C2A–C2B* mutant restored the small-sized vesicles, while the functional C2B domain is sufficient to rescue the large-sized vesicles (Fig. 5 B–E and G–L), confirming redundant roles of both C2 domains in CME and the critical role of the C2B domain in bulk endocytosis. In addition, the KKAA mutation prevented Syt1 from rescuing the small-sized, but not large-sized, endocytic vesicles (Fig. 5 F–L). Altogether, Syt1 functions as a Ca^{2+} sensor facilitating CME but clamping bulk endocytosis to ensure a precise coupling of endocytosis to exocytosis during both somatic secretion and synaptic transmission.

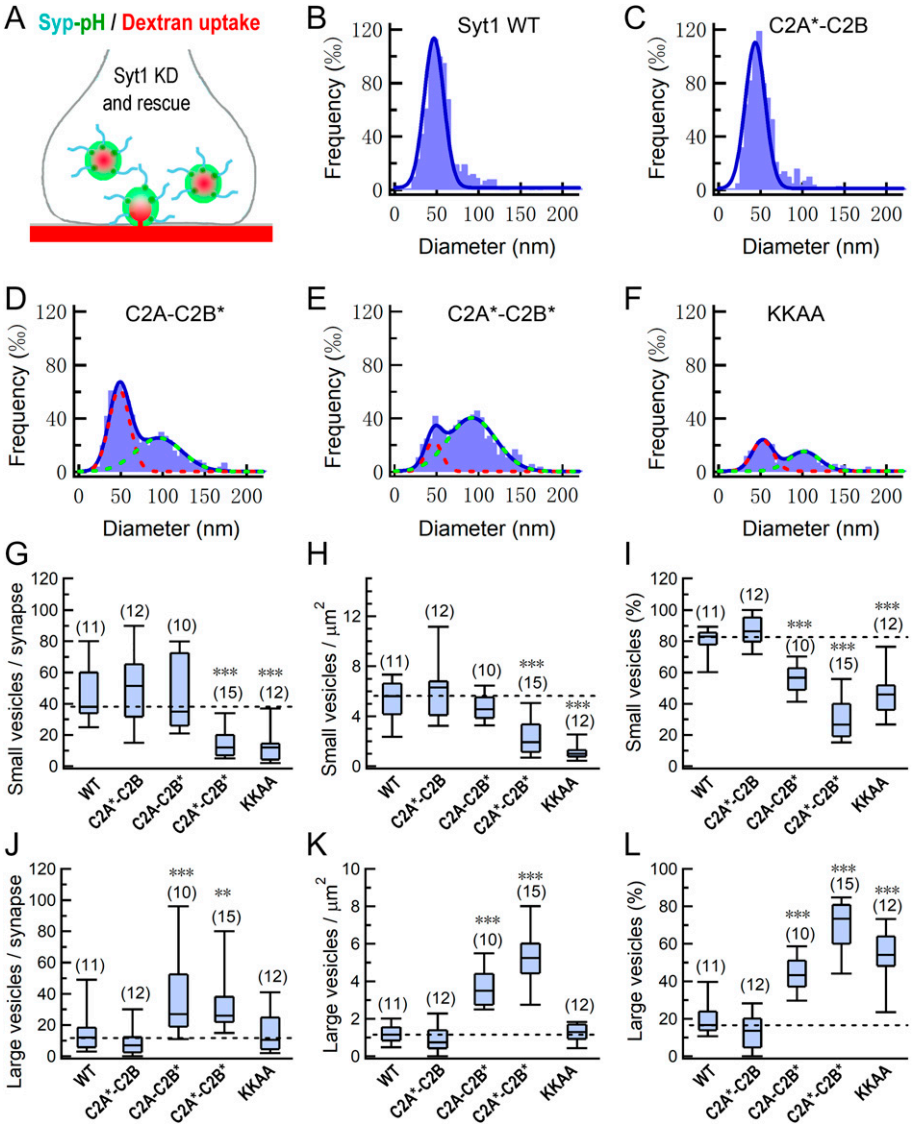

Fig. 5. Syt1 is a Ca^{2+} sensor facilitating CME but inhibiting bulk endocytosis in synaptic boutons. (*A*) Cartoon illustration of STED imaging of Syp–pH and endocytosed dextran (10 kDa) in Syt1-KD hippocampal synaptic boutons with the rescue of indicated Syt1 mutants. (*B–F*) Histograms showing the diameter distribution of endocytic vesicles (dextran-positive) in Syt1-KD boutons with the rescue of indicated Syt1 mutants following 70 mM KCl stimulation (2 min). The dashed and solid traces are the individual and overall fits to single or multiple (C2A–C2B*, C2A*–C2B*, KKAA) Gaussian functions. (*G–L*) Statistics of small ($\Phi \leq 65$ nm) and large ($\Phi > 65$ nm) endocytic vesicles in Syt1-KD and rescue boutons as in *B–F*. Data were collected from four independent experiments and analyzed by one-way ANOVA; $^{**}P < 0.01$, $^{***}P < 0.001$.

Syt1 Ca^{2+} Dependently Mediates Membrane Tubulation and Remodeling. To understand why the Ca^{2+}-binding site of the C2B domain but not C2A domain is critical for the inhibitory role of Syt1 on bulk endocytosis, we tested the ability of different C2 domains of Syt1 to induce membrane curvature with in vitro liposome manipulation and negative stain electron microscopy. As expected, the wild-type C2A–C2B fragment (with the transmembrane domain truncated) converted liposomes into long, thin lipid tubules in the presence of 1 mM Ca^{2+} but not in the Ca^{2+}-free and 1 mM ethylene glycol-bis (β-aminoethyl ether)-N,N,N′,N′-tetraacetic acid (EGTA)–containing bath solution (Fig. 6 A and B). Similar to a previous report (36), the fraction of tubulated liposomes decreased greatly for Syt1 mutants with the Ca^{2+}-binding ability of either C2A or C2B domain abolished (Fig. 6 A and B). Although C2A*–C2B and C2A–C2B* fragments exhibited similar defects in membrane tubulation, interestingly, the tubulated liposomes showed differences in that the C2A*–C2B kept its ability to convert liposomes into thin tubules, but the C2A–C2B* showed much more thick tubules (Fig. 6 A–D). In addition, C2A*–C2B* exhibited a similar level of thick tubules as C2A–C2B*, and KKAA showed a similar level of thick tubules as C2A*–C2B (Fig. 6 A–D). These data indicate that the C2B domain of Syt1 has stronger tubulation activity than the C2A domain and thus can effectively convert the thick tubules into thin ones, which may explain why the C2B domain of Syt1 is essential to inhibit bulk endocytosis.

Ca^{2+}-Binding and Non-Ca^{2+}–Binding Syts Cooperate to Regulate Endocytosis. Although we have revealed the molecular mechanism for Ca^{2+} inhibition in endocytosis, a conspicuous question of why the inhibitory effect is only observed in few preparations remains to be resolved (6–8, 12, 13). Similarly, we did not observe Ca^{2+} inhibition in endocytosis in control DRG neurons (*SI Appendix*, Fig. S12 *A* and *B*). Considering that Syt11, a highly expressed non-Ca^{2+}–binding Syt in DRG neurons, constitutively inhibits both CME and bulk endocytosis (25, 28), we tested the Ca^{2+} dependency of C_m

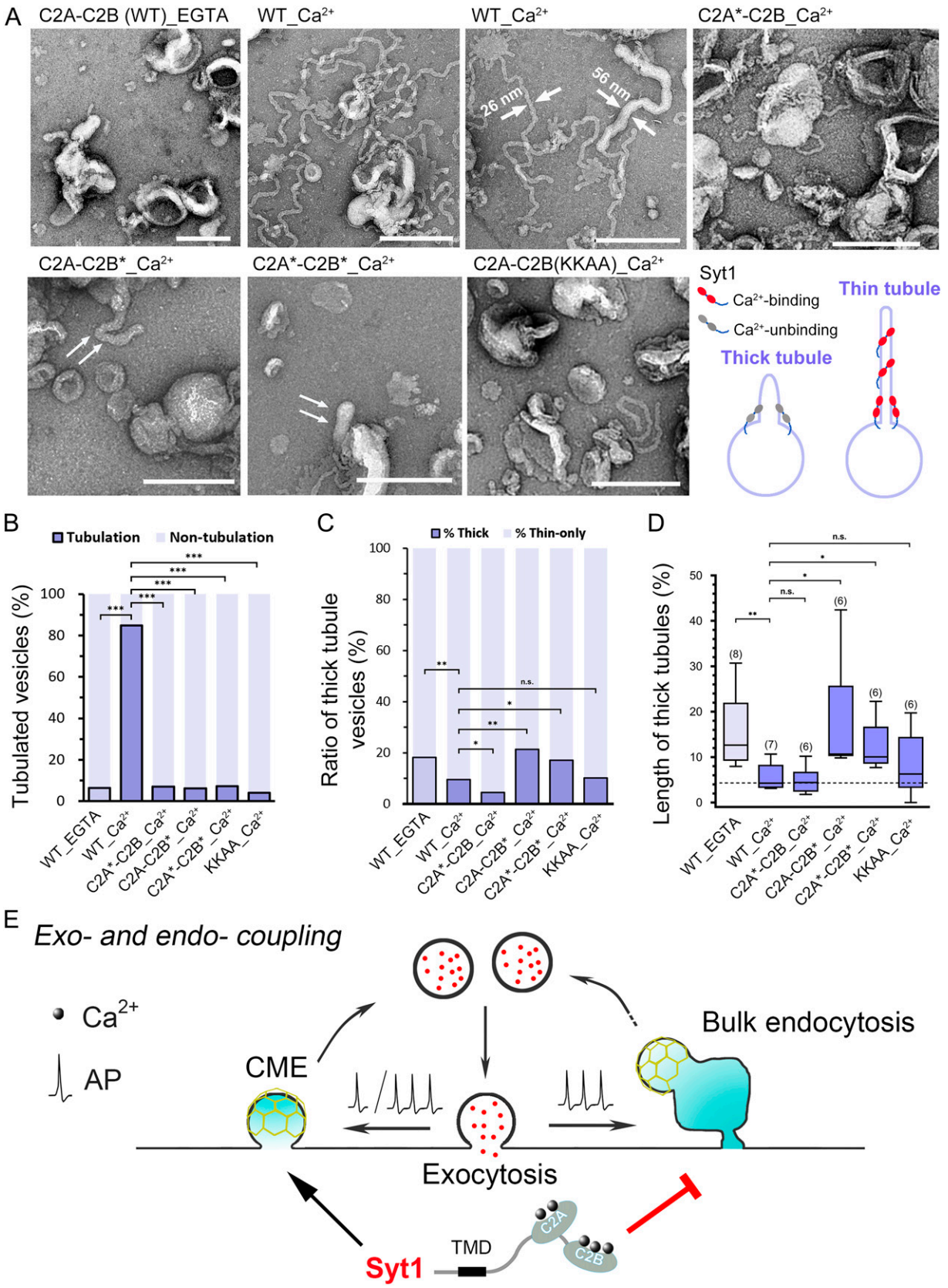

Fig. 6. Syt1 Ca^{2+}-dependently mediates membrane invagination. (*A*) Electron micrographs of liposomes incubated with the indicated Syt fragments in the presence or absence of Ca^{2+}. Two types of tubules were observed, long thinner tubules (*Φ*~26 nm) and short thicker tubules (*Φ*~56 nm, double arrows). (Scale bars, 400 nm.) (*B*–*D*) Quantification of tubulated liposomes (*B*), thick tubule–containing liposomes (*C*), and length of thick tubules (*D*) obtained under the indicated conditions. (*E*) Working model showing bidirectional roles of Syt1 as a Ca^{2+} sensor to regulate neural endocytosis. Syt1 functions as a primary Ca^{2+} sensor facilitating CME to ensure highly efficient vesicle recycling but inhibiting bulk endocytosis probably through membrane manipulation to achieve both efficient and precise exocytosis–endocytosis coupling during neurotransmission; AP, action potential; TMD, transmembrane domain. In the box plots, the central line of each box represents the median, the edges of the box represent the 25th and 75th percentiles, and the whiskers extend to 5% and 95% the most extreme data points. Data were collected from three independent experiments and were analyzed by Pearson's χ^2 analysis for *B* and *C* and one-way ANOVA for *D*; $*P < 0.05$, $**P < 0.01$, $***P < 0.001$.

decay in the absence of this constitutive brake of endocytosis. As expected, the C_m decay in control neurons was accelerated substantially with a smaller time constant (τ) by increasing membrane depolarization from 100 ms to 200 ms (*SI Appendix*, Fig. S12 *A* and *B*). Consistent with our previous findings (25), the C_m decay in Syt11-KD neurons fitted well to a double-exponential decay function (*SI Appendix*, Fig. S12*C*), representing accelerated bulk endocytosis and CME. Strikingly, the initial phase of exocytosis–endocytosis was slowed down, while the subsequent slow phase accelerated significantly following the increased pulse stimulation (*SI Appendix*, Fig. S12 *C–G*), indicating that increased Ca^{2+} influx inhibits the fast component but promotes the slow phase of endocytosis in the absence of Syt11. Thus, this work provided an insightful mechanism that the apparent conflict effects of Ca^{2+} on endocytosis in different preparations is probably due to different expression patterns of Ca^{2+}-sensing proteins (e.g., calmodulin and Syt1) and non-Ca^{2+}–binding Syts (e.g., Syt11 as a constitutive brake) that cooperate to provide a diversified precise regulation of exocytosis–endocytosis coupling.

Discussion

Endocytosis is spatiotemporally coupled to exocytosis in neurons and endocrinal cells, while machineries and regulators involved in the coupling remain elusive. Both positive (8, 9, 37) and negative (12, 13) roles of neural activity/Ca^{2+} in endocytosis have been reported, making the endocytic role of Ca^{2+} a four-decades–long dispute (1, 2, 4, 6). In contrast to the well-established Ca^{2+} sensors (calmodulin and Syt1) that promote endocytosis, the Ca^{2+}-dependent inhibitor(s) for endocytosis have never been reported. Here, we identify Syt1 as a primary Ca^{2+} sensor to facilitate CME for efficient vesicle recycling but surprisingly inhibit bulk endocytosis to prevent excessive membrane retrieval especially during sustained neuronal activity (Fig. 6E). Thus, the balance between the facilitatory and inhibitory effects of Syt1 on endocytosis offers a fine-tuning mechanism to ensure both the efficient and precise coupling of endocytosis to exocytosis especially during bursting activity, which is essential for maintaining sustainable secretion and a stable membrane structure.

The primary finding of the present work is the bidirectional role of Syt1 in exocytosis–endocytosis, which is supported by the following evidence: 1) the fluorescence decay of Syp–pH in Syt1-KD synaptic boutons was decreased upon 45 mM KCl stimulation but accelerated in response to 70 mM KCl stimulation (Fig. 1 A–E and *SI Appendix*, Fig. S3); 2) Syt1 KD speeded up the fast phase but slowed down the slow phase of Syp–pH fluorescence decay upon 70 mM KCl stimulation (Fig. 1 C–H); 3) Syt1 KD substantially increased the fraction of Syp–pH fluorescence overshoot (Fig. 1 I and J); 4) a similar phenomenon was also observed in primary sensory DRG neurons via C_m recordings (*SI Appendix*, Fig. S5); 5) Syt1 KD decreased the small-sized but increased the large-sized endocytic vesicles in synaptic boutons (Fig. 2); 6) synaptic endocytosis in Syt1-KD neurons was reproduced in Syt1-cKO boutons (Fig. 3 and *SI Appendix*, Fig. S7); 7) Tf uptake was Ca^{2+} dependent and decreased in Syt1-KD neurons (Fig. 4 A–F); 8) Ca^{2+}-dependent large dextran uptake was increased in Syt1-KD neurons and restored by full-length Syt1 (Fig. 4 G–J); 9) the Ca^{2+}-binding abilities of C2A and C2B domains are redundant for Syt1 to promote Tf uptake (Fig. 4F) while that of the C2B domain is critical for Syt1 to inhibit large dextran uptake (Fig. 4J); 10) the Ca^{2+}-binding ability is similarly required for Syt1 to promote small-sized endocytic vesicles (Fig. 5 G–I) but inhibit large-sized endocytic vesicles during synaptic transmission (Fig. 5 J–L); and 11) Syt1 Ca^{2+} dependently mediates membrane tubulation and curvature (Fig. 6 A–D). Together, these findings demonstrate that Syt1 serves as a primary Ca^{2+} sensor to promote CME but clamp bulk endocytosis.

Unlike Ca^{2+} sensors that accelerate endocytosis (1, 2, 9), Ca^{2+}-dependent inhibitors for endocytosis have never been reported, leaving the mechanism of Ca^{2+} inhibition in endocytosis a long mystery. Recently we have shown that Syt11 serves as a Ca^{2+}-independent inhibitor for endocytosis (3, 19, 25, 28). Here, we defined that Syt1, the primary Ca^{2+} sensor initiating SNARE-dependent vesicular exocytosis (38–41) and a well-established Ca^{2+} sensor that promotes CME (3, 5, 16, 18, 24, 34), also functions as the primary Ca^{2+} sensor clamping endocytosis during sustained neuronal activity, the disruption of which leads to excessive membrane retrieval. Recently, emerging evidence has shown that temperature is an important factor involved in exocytosis–endocytosis coupling, and clathrin may mediate endocytosis mainly at room temperature, whereas ultrafast endocytosis is dominant at physiological temperature (27, 42). To further confirm the endocytic role of Syt1 at physiological temperature, we performed Syp–pH imaging, Tf uptake, dextran uptake, HRP uptake, and electron microscopy imaging and found that Syt1 has similar bidirectional effects on endocytosis at physiological temperature (37 °C) as at room temperature (Figs. 3 N–P and 4 and *SI Appendix*, Fig. S7). Considering that bulk endocytosis and the recently defined ultrafast endocytosis share multiple similarities (27, 42) (e.g., fast speed, large size, and clathrin-dependent regeneration of synaptic vesicles from endocytic endosomes), it will be of interest to study the effect of Syt1 on ultrafast endocytosis in the future. Nonetheless, this work uncovered the mechanisms underlying Ca^{2+} inhibition in endocytosis.

Structure–functional analysis revealed that the Ca^{2+}-binding capacity of C2A and C2B domains are redundant for Syt1 to promote CME, while the inhibition of bulk endocytosis is only critically dependent on the Ca^{2+}-binding ability of the C2B, but not the C2A, domain (Figs. 4 and 5). In addition, the conserved poly-lysine region KKAA in the C2B domain is essential for CME but not bulk endocytosis (Figs. 4 and 5), which is consistent with the report that Syt1 promotes CME through direct binding to AP-2 and stonin-2 via its poly-lysine region (24). The redundant role of C2A and C2B in CME is also consistent with a previous study in which the function of Syt1 in exocytosis and endocytosis was decoupled (16). Regarding the essential role of the C2B domain in bulk endocytosis, our in vitro data of liposome manipulation indicate that the C2B domain of Syt1 has stronger tubulation activity than the C2A domain and thus can effectively convert the membrane into thin tubules, which may explain the Ca^{2+}-dependent inhibition of Syt1 in bulk endocytosis. During elevated neuronal activity, accumulated Ca^{2+} activates calmodulin/calcineurin-dependent bulk endocytosis, which is restrained by the C2B domain of Syt1 because of its tubulation activity. Thus, the inhibitory effect of Syt1 only comes into play when bulk endocytosis is triggered, for instance under intense stimulation (Figs. 1–3) or following decreased Syt 11 expression (*SI Appendix*, Fig. S9 and ref. 25).

Considering the possible overlapping function of different Syt isoforms, we further compared the rescue effects of other Ca^{2+}-binding Syts, for example, Syt2 and Syt7 in Syt1-KD neurons. Interestingly, Syt2 showed only a partial rescue effect on both the fast and the slow phases of exocytosis–endocytosis

in Syt1-KD neurons (*SI Appendix*, Fig. S13). By contrast, Syt7 fully rescued the fast component but only partially rescued the slow component (*SI Appendix*, Fig. S13). These results indicate that, similar to their compensatory roles as Ca^{2+} sensors initiating exocytosis (41, 43–46), different Syt isoforms may play similar, but not exactly the same, roles in different endocytic pathways and may coordinate to regulate exocytosis–endocytosis coupling in response to different neural activity. In contrast to the Ca^{2+}-dependent bidirectional roles of Syt1 and other Ca^{2+}-binding Syts in exocytosis–endocytosis, the non-Ca^{2+}–binding Syt11 (41, 47, 48) constitutively inhibits CME and bulk endocytosis (25, 28). The architecture basis and kinetic changes of Syt proteins during distinct endocytic pathways should be new fundamental questions deserving extensive and systematic studies in the future.

Collectively, these findings define a fine-tuning mechanism of Ca^{2+}-dependent neuronal endocytosis that requires coordination of the primary Ca^{2+} sensors (e.g., Syt1 and calmodulin) and non-Ca^{2+}–binding Syts (e.g., Syt11 as a constitutive brake). Syt1 functions as a positive regulator to accelerate CME to ensure an efficient exocytosis–endocytosis. Following elevated neural/Ca^{2+} activity, calmodulin functions as a positive regulator to initiate bulk endocytosis, whereas Syt1 in turn serves as a negative regulator to clamp bulk endocytosis to prevent excessive membrane retrieval. This working model explains how neurons keep the precise coupling of endocytosis to exocytosis even during elevated activity. Our findings have not only uncovered a molecular mechanism for the Ca^{2+}-dependent inhibition of endocytosis but also provided a general membrane-remodeling working model for membrane fusion–fission regulation, which will probably end the four-decades–long dispute about the facilitatory (8, 9) and inhibitory (12, 13) role of Ca^{2+} in vesicular endocytosis.

Methods

Plasmids and Virus. The full-length rat Syt1 (NM_001033680) was subcloned into pCMV5 (Clontech). The nucleotide target sequence, G CAA ATC CAG AAA GTG CAA GT (shSyt1), was chosen to silence the expression of Syt1. A random sequence, TTC TCC GAA CGT GTC ACG T, which was predicted to target no genes in human, rat, and mouse cells, was chosen as a negative control (Guangzhou Ribo Bio Co., Ltd). Annealed double-stranded oligonucleotides encoding the target sequences were inserted into the vector pRNAT-H1.1-RFP/GFP to generate plasmids expressing shRNAs against Syt1. An RNA interference (RNAi) shSyt1-resistant form of rSyt1 for the rescue experiments was generated by introducing the following silent mutations: G CAG ATT CAA AAG GTT CAA GT. The D230, 232N mutant (C2A*), D363, 365N mutant (C2B*), D230, 232, 363, 365N mutant (C2A*–C2B*), K345 and 346A mutant (KKAA) were generated from the RNAi-resistant form of Syt1. All mutants were produced by PCR using the QuikChange site-directed mutagenesis kit (Stratagene). Syp–pH was kindly gifted by Yongling Zhu (The Salk Institute for Biological Studies). All constructs were verified by DNA sequencing. The AAV2/9-Syn-Cre virus was from Shanghai Heyuan Biotech, and AAV2/9-Syn-DIO-Syp-pHluorin virus was produced and verified by Hanbio Biotechnology Co., Ltd.

Antibodies. The primary antibodies used for Western blotting and immunofluorescence were anti-actin (A5316, Sigma) and anti-Syt1 (105311, Synaptic System). The secondary antibody used for Western blotting was IRDye 680CW goat anti-mouse IgG (LIC-926-32220, LI-COR Biosciences), and the secondary antibody used for immunofluorescence staining was Alexa Fluor 488 goat anti-mouse IgG (H+L) (A11029) from Invitrogen.

Animals. The floxed Syt1-null transgenic mice were kindly gifted by Peng Cao (National Institute of Biological Sciences) with the permission of Thomas C. Sudhof (Stanford University School of Medicine). Adult Wistar rats (male, ∼60 g) were used for DRG neuron isolation, and postnatal day 0 to 1 Wistar rats or Syt1-null mice were used for hippocampal neuron culture. All animals were housed in an animal facility under a 12-h light/12-h dark cycle at 22 ± 2 °C with food and water available ad libitum. The use and care of animals were approved and directed by the Animal Care and Use Committee of Xi'an Jiaotong University and Peking University and the Association for Assessment and Accreditation of Laboratory Animal Care International.

Cell Culture and Transfection. DRG neurons were isolated as previously described (25, 49, 50). Briefly, adult Wistar rats (male, ∼60 g) were used, and DRGs were isolated in ice-cold L15 medium (Gibco). The ganglia were treated with trypsin (0.3 mg/mL) and collagenase (1 mg/mL) for 40 min at 37 °C. Cells were dissociated, collected, and transfected with the Neon 100-μL transfection system MPK10096 (Invitrogen). Cells were plated on poly-L-lysine–coated (Sigma) coverslips and maintained in Dulbecco's modified Eagle medium (DMEM)-F12 (Gibco) supplemented with 10% fetal bovine serum (FBS; Gibco). For gene-silencing experiments, 24 h after transfection, the culture medium was replaced by Neurobasal-A (Gibco, 10888-022) supplemented with 2% B27 (Gibco, 17504044), 0.5 mM L-glutamine (Gibco, 12403-010), 10 ng/mL nerve growth factor (Sigma, N8133), and 5 μM cytosine arabinoside (Sigma, C6645).

Hippocampal neurons were prepared and cultured as described previously (25, 28). Briefly, hippocampi were dissected from postnatal day 0 to 1 Wistar rats and treated with 0.25% trypsin at 37 °C for ∼12 min. Cells were plated on polyethyleneimine-coated glass coverslips and maintained in DMEM (Gibco) supplemented with 10% FBS for 3 h, which was then replaced by Neurobasal (Gibco) supplemented with 2% B27, 0.5 mM L-glutamine, and 5 μM cytosine arabinoside. Cultures at 5 d in vitro (DIV 5) were transfected by using a calcium-phosphate transfection method. Briefly, plasmids in a 250 mM $CaCl_2$ solution were slowly added to Hank's balanced salt solution and incubated at room temperature for 25 min. The mixture solution was then added to the culture and incubated for 15 min. The cells were washed with $MgCl_2$-containing medium and maintained in the original medium. Confocal imaging was performed at DIV 14.

C_m Recording. C_m was measured under the whole-cell configuration using an EPC10/2 amplifier controlled by Pulse software (HEKA Elektronik) as described previously (3, 25). The membrane potential was clamped at −70 mV, and pipette resistance was controlled between 3 and 4 MΩ. The external solution contained, in mM, 150 NaCl, 5 KCl, 2.5 $CaCl_2$, 1 $MgCl_2$, 10 4-(2-hydroxyethyl)-1-piperazineethanesulfonic acid (H-HEPES), and 10 D-glucose, pH 7.4. The intracellular pipette solution contained, in mM, 153 CsCl, 1 $MgCl_2$, 10 H-HEPES, and 4 Mg-ATP, pH 7.2. All recordings were performed at room temperature (22 to 25 °C). All chemicals were from Sigma unless otherwise indicated. Igor software (Wavemetrics) was used for all offline data analysis, and series conductance (G_s) and membrane conductance (G_m) were used to monitor the seal condition in the patch clamp recordings. Measurement of bulk endocytosis, which was reflected as a brief downward capacitance shift, was performed as previously described (9, 25). Capacitance traces were low-pass filtered at 30 Hz, and the brief downward capacitance shift was identified when the size of the capacitance decay was >20 fF and the decay rate was >50 fF/100 ms, with unchanged G_s and G_m.

Ca^{2+} Imaging. Cytosolic Ca^{2+} was measured with the Ca^{2+} indicator Fura-2 AM or Fluo-4 AM (Invitrogen) as previously described (25). For photometric measurement of $[Ca^{2+}]_i$, DRG neurons were loaded with 5 μM Fura-2 AM for 10 min at 37 °C and then washed three times with normal external solution at room temperature. $[Ca^{2+}]_i$ was measured by epifluorescence imaging using an Olympus IX-70 inverted microscope equipped with a monochromator-based system (TILL Photonics). X-chart software (HEKA Elektronik) was used to collect imaging data. $[Ca^{2+}]_i$ was calculated from the ratio (R) of the fluorescent signals excited at 340 nm and 380 nm with the following equation: $[Ca^{2+}]_i = K_d \times (R - R_{min})/(R_{max} - R)$, where K_d, R_{min}, and R_{max} are constants obtained from in vitro calibration.

For confocal $[Ca^{2+}]_i$ imaging of hippocampal neurons, cells were loaded with 5 μM Fluo-4 AM for 10 min at 37 °C and then imaged with a ×63 oil lens of a Zeiss 700 inverted confocal microscope. By using a gravity-fed perfusion system (MPS-2, Yibo Inc.), the 45 mM or 70 mM KCl–containing external solution was locally applied to evoke the $[Ca^{2+}]_i$ rise. Images were processed with ImageJ (NIH) and Adobe Photoshop (Adobe Systems, Inc.).

Gel Electrophoresis and Western Blotting. Cells were washed with phosphate-buffered saline (PBS) and homogenized on ice with lysate buffer (20 mM HEPES at pH 7.4, 100 mM KCl, 2 mM EDTA, 1% Nonidet P-40, 1 mM phenylmethylsulfonyl fluoride [PMSF], and 2% proteinase inhibitor [539134, Calbiochem]). The homogenates were centrifuged at 16,000 × *g* for 15 min at 4 °C, and the supernatants were collected and boiled in sampling buffer. Proteins were electrophoresed and transferred to nitrocellulose filter membranes. The membranes were blocked for 1 h in PBS containing 0.1% Tween-20 (vol/vol) and 5% nonfat dried milk (wt/vol). After washing with 0.1% Tween-20–containing PBS (PBST), the blots were incubated with primary antibodies at 4 °C overnight in PBST containing 2% bovine serum albumin (BSA). Secondary antibodies were then applied at room temperature for 1 h. Blots were scanned with an Odyssey infrared imaging system (LI-COR Biosciences) and quantified with ImageJ (NIH).

Immunofluorescence. Cells were fixed with 4% paraformaldehyde for 20 min and permeabilized with 0.3% Triton X-100 in PBS containing 2% BSA for 5 min at room temperature. After blocking for 1 h with 2% BSA in PBS, cells were incubated for 1 h with primary antibodies, washed three times with blocking solution, and incubated for 1 h with secondary antibodies. After three washes in blocking solution and one wash in PBS, cells were mounted on slides with 50% glycerol. A *z* series of 1-μm optical sections was scanned through the ×63 oil lens of a Zeiss 710 inverted confocal microscope. Images were processed in the Zeiss LSM Image Browser (version 3.0) and Adobe Photoshop (Adobe Systems, Inc.).

Tf Uptake. Cells were washed with serum-free DMEM containing 20 mM HEPES, pH 7.4, and 1 mg/mL BSA and serum starved in the same medium for 45 min at 37 °C. Cells were then incubated in serum-free medium containing 25 μg/mL human Tf conjugated to Alexa Fluor 594 (Invitrogen, T-13343) for 30 min at 37 °C. The unbound Tf was washed away with ice-cold PBS containing 0.3 mM $CaCl_2$ and 0.3 mM $MgCl_2$, and the cells were fixed with an ice-cold solution of 4% formaldehyde and processed for microscopy.

Dextran Uptake. Cells were incubated in 20 μM tetramethylrhodamine-dextran (10 kDa or 40 kDa)–containing extracellular solution (150 mM NaCl, 15 mM KCl, 2.5 mM $CaCl_2$, 1 mM $MgCl_2$, 10 mM H-HEPES, and 10 mM D-glucose, pH 7.4.) at 37 °C for 5 min. Dextran was washed from the cultures five times after incubation. For 100 mM K^+ external solution, the NaCl concentration was reduced to maintain the same ionic strength. Confocal slices were *z*-stack scanned on the Leica TCS SP8 STED 3X confocal microscope, and total dextran signals in the cell body were measured with ImageJ.

Confocal and STED Imaging. Hippocampal neurons were continuously perfused with standard bath solution containing 140 mM NaCl, 5 mM KCl, 2 mM $CaCl_2$, 2 mM $MgCl_2$, 10 mM H-HEPES, 10 mM D-glucose, 10 μM 6-cyano-7-nitroquinoxaline-2,3-dione (CNQX), and 50 μM D-2-amino-5-phosphonovaleric acid (D-AP5), pH 7.4. Standard 45 mM or 70 mM KCl–containing external solution was locally applied to the imaging area by using a gravity-fed perfusion system (MPS-2, Yibo Inc.). Time-lapse images were captured at 0.5-s intervals through the ×63 oil immersion lens of the Zeiss 700 confocal microscope. Fluorescence changes at individual boutons were monitored over time and calculated as normalized $\Delta F/F_0$. Images were acquired for 20 s before stimulation to establish a stable baseline.

STED images were acquired with a Leica TCS SP8 STED 3X microscope operated with the LAS-AX imaging software. Confocal and STED images were captured through an oil-immersion STED white lens (HC PL APO ×100/1.40). Syp–pH and dextran fluorescence were sequentially excited with a tunable white light laser at 488 nm and 594 nm, with the STED achieved by using a 592-nm or 660-nm depletion beam, and the restricted emission was collected with Leica HyD hybrid detectors at 490 to 560 nm and 600 to 650 nm, respectively. All STED images were deconvolved using Huygens software (Scientific Volume Imaging) and offline analyzed with LAS AF Lite (Leica).

HRP Uptake and Electron Microscopy. HRP uptake and electron microscopy of hippocampal neurons were performed as described previously (25). Neurons were washed three times with standard external solution and incubated with standard or 100 mM K^+ external solution supplemented with 10 mg/mL HRP at 37 °C for 2 min. Cells were then fixed in 2.5% glutaraldehyde and 2% paraformaldehyde in 0.1 M phosphate buffer (PB) for at least 30 min at room temperature. After washing with 100 mM Tris (pH 7.4), the cells were exposed to 0.1% diaminobenzidine and 0.2% H_2O_2 in 100 mM Tris for 4 to 5 min and washed with 100 mM Tris (pH 7.4). Cells were postfixed for 30 min with 2% osmium tetroxide and 1.5% potassium ferrocyanide in 0.1 M PB, washed, dehydrated through an ethanol series, embedded in Epon, and polymerized at 60 °C for 36 h. The embedded samples were separated from the dishes by dipping in liquid nitrogen and hot water. Cells of interest were isolated and mounted on prepolymerized Epon blocks. Ultrathin sections (~80 nm) were cut parallel to the cell monolayer, collected on single-slot, formvar-coated copper grids, and stained with 2% uranyl acetate for 30 min and 0.5% lead citrate for 15 min. Samples were observed in a Tecnai G2 20 200-kV transmission electron microscope at 120 kV. Electron microscopy of DRG neurons was similar but with no HRP uptake and diaminobenzidine staining. Docked vesicles were identified as those without any measurable distance from the plasma membrane. Vesicle diameters and numbers of HRP-labeled vesicles and endosomes were measured manually with the Zeiss LSM Image Browser (version 3.0).

In Vitro Liposome Tubulation Assay. Rat Syt1 cytosolic domain proteins were expressed and purified from *Escherichia coli*. Briefly, Syt1 C2A–C2B wild type (96 to 421) and mutants were cloned to pGEX-KG. Constructs were transformed into *E. coli* BL21 (DE3) and cultured in lysogeny broth medium at 37 °C to an optical density of 1.0, and protein expression was induced by 0.5 mM isopropyl β-D-1-thiogalactopyranoside at 18 °C for 10 h. Cells were collected by centrifugation at 8,000 × *g* for 5 min and suspended in lysis buffer (50 mM HEPES pH 7.4, 500 mM NaCl, 5% glycerol, 5 mM β-mercaptoethanol, and 1 mM PMSF) followed by sonication. Cell lysates were centrifuged at 15,000 × *g* for 45 min (twice), and supernatants were incubated with glutathione Sepharose beads (GE Healthcare) at 4 °C for 2 h. Beads were collected by centrifugation at 400 × *g* for 3 min and washed thoroughly with 10 μg/mL DNase I– and 10 μg/mL RNase I–containing binding buffer (50 mM HEPES pH 7.4, 100 mM NaCl, and 1 mM β-mercaptoethanol). Beads were then incubated with thrombin (Sigma-Aldrich) in binding buffer and digested at room temperature for 30 min. Flow-throughs were collected and concentrated to 0.5 to 1 mg/mL.

Liposomes constructed in vitro were composed of 50% brain total lipid extract + 45% dioleoylphosphatidylserine + 5% $PI(4,5)P_2$ (Avanti). Lipids dissolved in chloroform were vacancy dried and resuspended in binding buffer at a concentration of 0.5 mg/mL. After 15 freeze–thaw cycles, vesicles were extruded through 400-nm–pore size polycarbonate filters for another 15 cycles.

For transmission electron microscopy imaging of vesicle tubulation, 4 μM Syt1 wild-type or mutant proteins were mixed with liposomes in the presence of 1 mM EGTA or 1 mM $CaCl_2$ at room temperature for 1 h and plated on the glow-discharged (10 mA for 10 s) 400-mesh carbon film copper grids. Following two 1-s washes in double-distilled water, proteins were negatively stained in 1% uranyl acetate for 30 s. Samples were observed on a 200-kV FEI Talos F200C transmission electron microscopy in the Instrumental Analysis Center of Xi'an Jiaotong University, and images were acquired via a fast Ceta 16M complementary metal oxide semiconductor (CMOS) camera.

Statistics. All experiments were replicated at least three times. Sample sizes are consistent with those reported in similar studies. No samples or recordings that provided successful measurements were excluded from analysis. Experiments did not involve blinding because we used green fluorescent protein as a marker for transfection and compared recordings from the same neurons following different treatments. Data are shown as mean ± SEM or box plots. For box plots, the central lines represent the median, the edges represent the interquartile ranges, and the whiskers represent the overall distribution. All data were tested for normality by the Shapiro–Wilk test before the statistical analysis. Statistical comparison was performed with a two-tailed unpaired/paired Student's *t* test, a Wilcoxon–Mann–Whitney nonparametric test, a Fisher's exact test, or a one-way ANOVA followed by Tukey's multiple comparisons test as indicated. All tests were conducted using SPSS 13.0. Significant differences were accepted at $P < 0.05$. Numbers of cells/boutons analyzed are indicated in the figures or legends.

Data Availability. All study data are included in the article and/or *SI Appendix*.

ACKNOWLEDGMENTS. We thank Drs. Jianyuan Sun (Institute of Biophysics, Chinese Academy of Science), Chen Zhang (Capital Medical University, China), Xuelin Lou (Medical College of Wisconsin), and Jun Yao (Tsinghua University) for discussion and comments, Peng Cao (National Institute of Biological Sciences, Beijing, China) and Thomas C. Sudhof (Stanford University School of Medicine) for the floxed Syt1-null mice, Yingchun Hu (Core Facilities, College of Life Sciences, Peking University) for assistance with electron microscopy, and Iain C. Bruce (Peking University) for reading the manuscript. This work was supported by the National Natural Science Foundation of China (32171233, 81901308, 81974203, 31670843, 32000704, 31400708, 21790390, and 21790394), the Natural Science Foundation of Shaanxi Province of China (2019JC-07 and 2020JQ-029), the Science and Technology Innovation Projects of China (20-163-00-TS-009-035-01), the Natural Science Foundation of Sichuan Province of China (2020YJ0337 and 2020YJ0378), China Postdoctoral Science Foundation (2018M640972), and the Innovation Capability Support Program of Shaanxi Province, China (2021TD-37, 2018PT-28, and 2017KTPT-04).

Author affiliations: [a]Neuroscience Research Center, Institute of Mitochondrial Biology and Medicine, Key Laboratory of Biomedical Information Engineering of Ministry of Education, School of Life Science and Technology, Xi'an Jiaotong University, Xi'an 710049, China; [b]Department of Neurology, the First Affiliated Hospital of Xi'an Jiaotong University, Xi'an 710061, China; [c]Core Facilities Sharing Platform, Xi'an Jiaotong University, Xi'an 710049, China; [d]State Key Laboratory of Membrane Biology, Institute of Molecular Medicine, Peking University, Beijing 100871, China; [e]Peking-Tsinghua Center for Life Sciences, Peking University, Beijing 100871, China; [f]College of Life Sciences, Liaocheng University, Liaocheng 252059, China; [g]Haidu College, Qingdao Agricultural University, Qingdao 265200, China; [h]Key Laboratory of Medical Electrophysiology, Ministry of Education of China, Institute of Cardiovascular Research, Southwest Medical University, Luzhou 646000, China; and [i]College of Life Sciences, Forestry and Agriculture, Qiqihar University, Qiqihar 161004, China

Author contributions: C.W., Z.C., R.H., Z.Z., J. Liu, and J. Long designed research; Y.C., Z.C., S.H., X.W., R.H., Z.X., Y.W., B.W., X.L., Y.P., Y.G., K.H., J.H., A.W., C.B., Z.L., Q.S., H.X., X.K., and S.S. performed research; Y.C., Z.C., S.H., X.W., R.H., Z.X., Y.W., B.W., X.L., Y.P., Y.G., K.H., J.H., A.W., C.B., Z.L., Q.S., H.X., X.K., and S.S. analyzed data; C.W., Z.C., R.H., and Y.C. wrote the paper; and all authors reviewed the manuscript and approved the submission.

1. Y. Saheki, P. De Camilli, Synaptic vesicle endocytosis. *Cold Spring Harb. Perspect. Biol.* **4**, a005645 (2012).
2. L. G. Wu, E. Hamid, W. Shin, H. C. Chiang, Exocytosis and endocytosis: Modes, functions, and coupling mechanisms. *Annu. Rev. Physiol.* **76**, 301–331 (2014).
3. Z. Xie *et al.*, Molecular mechanisms for the coupling of endocytosis to exocytosis in neurons. *Front. Mol. Neurosci.* **10**, 47 (2017).
4. J. Leitz, E. T. Kavalali, Ca^{2+} dependence of synaptic vesicle endocytosis. *Neuroscientist* **22**, 464–476 (2016).
5. T. C. Südhof, Calcium control of neurotransmitter release. *Cold Spring Harb. Perspect. Biol.* **4**, a011353 (2012).
6. Q. Song, M. Huang, B. Wang, X. Kang, C. Wang, Bidirectional regulation of Ca^{2+} in exo-endocytosis coupling. *Sci. China Life Sci.* **61**, 1583–1585 (2018).
7. B. Ceccarelli, W. P. Hurlbut, Ca^{2+}-dependent recycling of synaptic vesicles at the frog neuromuscular junction. *J. Cell Biol.* **87**, 297–303 (1980).
8. N. Hosoi, M. Holt, T. Sakaba, Calcium dependence of exo- and endocytotic coupling at a glutamatergic synapse. *Neuron* **63**, 216–229 (2009).
9. X. S. Wu *et al.*, Ca^{2+} and calmodulin initiate all forms of endocytosis during depolarization at a nerve terminal. *Nat. Neurosci.* **12**, 1003–1010 (2009). Correction in: *Nat. Neurosci.* **13**, 649 (2010).
10. E. Neher, R. S. Zucker, Multiple calcium-dependent processes related to secretion in bovine chromaffin cells. *Neuron* **10**, 21–30 (1993).
11. J. Klingauf, E. T. Kavalali, R. W. Tsien, Kinetics and regulation of fast endocytosis at hippocampal synapses. *Nature* **394**, 581–585 (1998).
12. H. von Gersdorff, G. Matthews, Inhibition of endocytosis by elevated internal calcium in a synaptic terminal. *Nature* **370**, 652–655 (1994).
13. X. S. Wu, L. G. Wu, The yin and yang of calcium effects on synaptic vesicle endocytosis. *J. Neurosci.* **34**, 2652–2659 (2014).
14. T. A. Ryan *et al.*, The kinetics of synaptic vesicle recycling measured at single presynaptic boutons. *Neuron* **11**, 713–724 (1993).
15. H. Gad, P. Löw, E. Zotova, L. Brodin, O. Shupliakov, Dissociation between Ca^{2+}-triggered synaptic vesicle exocytosis and clathrin-mediated endocytosis at a central synapse. *Neuron* **21**, 607–616 (1998).
16. J. Yao, S. E. Kwon, J. D. Gaffaney, F. M. Dunning, E. R. Chapman, Uncoupling the roles of synaptotagmin I during endo- and exocytosis of synaptic vesicles. *Nat. Neurosci.* **15**, 243–249 (2011).
17. F. Deák, S. Schoch, X. Liu, T. C. Südhof, E. T. Kavalali, Synaptobrevin is essential for fast synaptic-vesicle endocytosis. *Nat. Cell Biol.* **6**, 1102–1108 (2004).
18. K. E. Poskanzer, K. W. Marek, S. T. Sweeney, G. W. Davis, Synaptotagmin I is necessary for compensatory synaptic vesicle endocytosis in vivo. *Nature* **426**, 559–563 (2003).
19. X. Wu, S. Hu, X. Kang, C. Wang, Synaptotagmins: Beyond presynaptic neurotransmitter release. *Neuroscientist* **26**, 9–15 (2020).
20. Y. C. Li, N. L. Chanaday, W. Xu, E. T. Kavalali, Synaptotagmin-1- and synaptotagmin-7-dependent fusion mechanisms target synaptic vesicles to kinetically distinct endocytic pathways. *Neuron* **93**, 616–631 (2017).
21. K. E. Poskanzer, R. D. Fetter, G. W. Davis, Discrete residues in the C_2B domain of synaptotagmin I independently specify endocytic rate and synaptic vesicle size. *Neuron* **50**, 49–62 (2006).
22. K. Nicholson-Tomishima, T. A. Ryan, Kinetic efficiency of endocytosis at mammalian CNS synapses requires synaptotagmin I. *Proc. Natl. Acad. Sci. U.S.A.* **101**, 16648–16652 (2004).
23. N. L. Kononenko *et al.*, Compromised fidelity of endocytic synaptic vesicle protein sorting in the absence of stonin 2. *Proc. Natl. Acad. Sci. U.S.A.* **110**, E526–E535 (2013).
24. V. Haucke, M. R. Wenk, E. R. Chapman, K. Farsad, P. De Camilli, Dual interaction of synaptotagmin with μ2- and α-adaptin facilitates clathrin-coated pit nucleation. *EMBO J.* **19**, 6011–6019 (2000).
25. C. Wang *et al.*, Synaptotagmin-11 inhibits clathrin-mediated and bulk endocytosis. *EMBO Rep.* **17**, 47–63 (2016).
26. E. L. Clayton *et al.*, Dynamin I phosphorylation by GSK3 controls activity-dependent bulk endocytosis of synaptic vesicles. *Nat. Neurosci.* **13**, 845–851 (2010).
27. S. Watanabe *et al.*, Ultrafast endocytosis at mouse hippocampal synapses. *Nature* **504**, 242–247 (2013).
28. C. Wang *et al.*, Synaptotagmin-11 is a critical mediator of parkin-linked neurotoxicity and Parkinson's disease-like pathology. *Nat. Commun.* **9**, 81 (2018).
29. G. Cheung, M. A. Cousin, Adaptor protein complexes 1 and 3 are essential for generation of synaptic vesicles from activity-dependent bulk endosomes. *J. Neurosci.* **32**, 6014–6023 (2012).
30. W. D. Zhao *et al.*, Hemi-fused structure mediates and controls fusion and fission in live cells. *Nature* **534**, 548–552 (2016).
31. W. Shin *et al.*, Visualization of membrane pore in live cells reveals a dynamic-pore theory governing fusion and endocytosis. *Cell* **173**, 934–945 (2018).
32. H. T. McMahon, E. Boucrot, Molecular mechanism and physiological functions of clathrin-mediated endocytosis. *Nat. Rev. Mol. Cell Biol.* **12**, 517–533 (2011).
33. E. L. Clayton, G. J. O. Evans, M. A. Cousin, Bulk synaptic vesicle endocytosis is rapidly triggered during strong stimulation. *J. Neurosci.* **28**, 6627–6632 (2008).
34. N. Jarousse, R. B. Kelly, The AP2 binding site of synaptotagmin 1 is not an internalization signal but a regulator of endocytosis. *J. Cell Biol.* **154**, 857–866 (2001).
35. C. A. Loewen, S. M. Lee, Y. K. Shin, N. E. Reist, C_2B polylysine motif of synaptotagmin facilitates a Ca^{2+}-independent stage of synaptic vesicle priming in vivo. *Mol. Biol. Cell* **17**, 5211–5226 (2006).
36. E. Hui, C. P. Johnson, J. Yao, F. M. Dunning, E. R. Chapman, Synaptotagmin-mediated bending of the target membrane is a critical step in Ca^{2+}-regulated fusion. *Cell* **138**, 709–721 (2009).
37. Z. He *et al.*, Ca^{2+} triggers a novel clathrin-independent but actin-dependent fast endocytosis in pancreatic beta cells. *Traffic* **9**, 910–923 (2008).
38. E. R. Chapman, Synaptotagmin: A Ca^{2+} sensor that triggers exocytosis? *Nat. Rev. Mol. Cell Biol.* **3**, 498–508 (2002).
39. N. Gustavsson, W. Han, Calcium-sensing beyond neurotransmitters: Functions of synaptotagmins in neuroendocrine and endocrine secretion. *Biosci. Rep.* **29**, 245–259 (2009).
40. T. C. Südhof, J. E. Rothman, Membrane fusion: Grappling with SNARE and SM proteins. *Science* **323**, 474–477 (2009).
41. Z. P. P. Pang, T. C. Südhof, Cell biology of Ca^{2+}-triggered exocytosis. *Curr. Opin. Cell Biol.* **22**, 496–505 (2010).
42. S. Watanabe *et al.*, Clathrin regenerates synaptic vesicles from endosomes. *Nature* **515**, 228–233 (2014).
43. C. Chen, P. Jonas, Synaptotagmins: That's why so many. *Neuron* **94**, 694–696 (2017).
44. J. Xu, T. Mashimo, T. C. Südhof, Synaptotagmin-1, -2, and -9: Ca^{2+} sensors for fast release that specify distinct presynaptic properties in subsets of neurons. *Neuron* **54**, 567–581 (2007).
45. T. Bacaj *et al.*, Synaptotagmin-1 and -7 are redundantly essential for maintaining the capacity of the readily-releasable pool of synaptic vesicles. *PLoS Biol.* **13**, e1002267 (2015).
46. A. C. Wolfes, C. Dean, The diversity of synaptotagmin isoforms. *Curr. Opin. Neurobiol.* **63**, 198–209 (2020).
47. C. von Poser, K. Ichtchenko, X. Shao, J. Rizo, T. C. Südhof, The evolutionary pressure to inactivate. A subclass of synaptotagmins with an amino acid substitution that abolishes Ca^{2+} binding. *J. Biol. Chem.* **272**, 14314–14319 (1997).
48. H. Dai *et al.*, Structural basis for the evolutionary inactivation of Ca^{2+} binding to synaptotagmin 4. *Nat. Struct. Mol. Biol.* **11**, 844–849 (2004).
49. C. Zhang, Z. Zhou, Ca^{2+}-independent but voltage-dependent secretion in mammalian dorsal root ganglion neurons. *Nat. Neurosci.* **5**, 425–430 (2002).
50. W. Lin *et al.*, Growth differentiation factor-15 produces analgesia by inhibiting tetrodotoxin-resistant Nav1.8 sodium channel activity in rat primary sensory neurons. *Neurosci. Bull.* **37**, 1289–1302 (2021).